nzsee
NEW ZEALAND SOCIETY FOR EARTHQUAKE ENGINEERING

Full waveform tomography for the upper South Island region, New Zealand

T.D Nguyen, B.A. Bradley, R.L. Lee
University of Canterbury, Christchurch.

R.W. Graves
U.S. Geological Survey, USA.

ABSTRACT

In this paper, we apply Full Waveform Tomography (FWT) based on the Adjoint-Wavefield (AW) method to iteratively invert an existing 3-D geophysical velocity model for the upper South Island region, New Zealand. Through the AW method, gradients of model parameters (compressional and shear wave velocities) were computed by implementing the cross-adjoint of forward and backward wave fields. We used L-BFGS/ line search algorithms to obtain a model update. For real data analysis, misfit measurements based on data from broadband stations were utilized. The misfit measure is a frequency-dependent multi-taper travel-time difference at periods from 10 - 40 s. After the iterative inversion, the simulated seismograms computed using our final velocity model shows good agreement to the observed data.

1 INTRODUCTION

A major goal of this study was to develop a crustal velocity model to improve the accuracy of earthquake ground motion simulations for use in physics-based seismic hazard models (Graves et al., 2011; Bradley et al., 2017) for New Zealand. In this paper, we apply Full Waveform Tomography (FWT) based on the Adjoint-Wavefield (AW) method. We introduce our numerical solver of the 3-D wave equation (forward simulation). We then review the concept of the AW method and introduce the adjoint simulation, sensitivity and Hessian kernel calculations and model updating.

We have employed the algorithms for data processing, waveform segmentation and misfit calculation/ adjoint source construction via a series of Python packages including *Pyflex* (Krischer et al., 2015b) and *Pyadjoint* (Krischeret al., 2015a). For broadband data analysis section, an iterative inversion run at frequency band 0.025-0.1 Hz was performed, using the multi-taper travel-time difference as measurement for the adjoint source (Tromp et al., 2005; Tape et al., 2009). An independent set of events was introduced for assessment of the model improvement using metrics such as relative waveform misfit and normalized cross-correlation coefficients.

2 METHODOLOGY

2.1 3-D wave simulation

To set up the full waveform tomography problem, first we need to solve the wave propagation or forward modelling. The stress-velocity formulation of 3-D visco-elastic wave equations (Virieux, 1986) has been solved numerically in software emod3d for a given velocity model using a finite different scheme (Graves, 1996). We use a point source with given centroid-moment tensor solution (Ristau, 2008) to represent the earthquake source. The damping boundary condition was implemented for a number of grid points near the external boundaries of the velocity model and the attenuation factors *Qs/Qp* were defined based on the initial *Vs/Vp* model but not updated along the inversion. This wave propagation modelling has been frequently used in physics-based probabilistic seismic hazard analysis applications (e.g. Cybershake, Graves (2011)).”

2.2 Multi-taper misfit and model update using AW method

For the optimization, we define a phase-difference misfit function χ_P between the observed data recorded at seismic stations and the simulated data from our forward simulation for different events. The other possible misfit function defined for the same observed and simulated data is χ_Q which relates to the amplitude difference. The phase-difference misfit function, according to an earth model m, measures frequency-dependent phase differences estimated with multi-taper approach as follows (Laske and Masters, 1996; Tape et al., 2007):

$$\chi_P(m) = \frac{1}{N_S}\sum_{i=1}^{N_S}\frac{1}{N_j}\sum_{j=1}^{N_j}\frac{1}{2}\int_{-\infty}^{\infty} W_{Pij}(\omega)\left[\frac{\tau_{ij}^{d}(\omega)-\tau_{ij}^{s}(\omega,m)}{\sigma_P(\omega)}\right]^2 d\omega \quad (1)$$

where N_S is number of events included in the inversion; N_j is number of windows picked for source *i*; W_{Pij} denotes the frequency taper for the frequency range of the measurements; $\tau_{ij}^{s}(\omega,m)$ and ; $\tau_{ij}^{d}(\omega)$ are the frequency-dependent phase measurements for the observed (*d*) and synthetic (*s*) data correspondingly; $\sigma_P(\omega)$ is the travel-time uncertainty introduced in making measurements (estimated by a cross-correlation method).

From the defined misfit function, we can construct the Frechet derivatives (Tarantola, 1984). We consider the AW method, which back-propagates the data differences to attract information of the medium (Tromp et al., 2005; Plessix, 2006). The adjoint sources are defined according to the multi-taper travel-time measurements.

After calculation of the sensitivity kernels for all events, we combine them and precondition by the sum of the approximate Hessian matrices (Shin et al., 2008; Zhu et al., 2015; Butzer, 2015) to compute the model update gradient. The gradient g then would be smoothed by convolution with a 3-D spatial Gaussian function (Tape et al., 2007). The horizontal and vertical widths of the Gaussian function are different (wider in horizontal directions) to speed up the misfit reduction as well as preserve the high variation with depth. The L-BFGS method (Nocedal and Wright, 2006; Zhu et al., 2015; Modrak et al., 2018) was implemented for model update, using Equation (2):

$$m_{k+1} = m_k - \alpha_k H_k g_k \quad (2)$$

where m_k is the current model at k^{th} iteration; α_k is the optimal step length for the model update determined by the parabola-fitting line search algorithm (Nocedal and Wright, 2006); H_k is the approximation of the inversed Hessian matrix; g_k is the current gradient. Here we store the inversed Hessian matrix implicitly by retrieving the model and gradient from n iterations (n > 2) before the current iteration. The approximated Hessian matrix reconstructed from L-BFGS method can be compared to the Hessian matrix directly calculated from Gauss-Newton method (Tran et al., 2020).

2.3 Data processing packages

To construct the adjoint source for backward simulation, we implement *Pyflex* - an automated time-window selection algorithm for seismic tomography (Maggi et al., 2009; Krischer et al.,2015b) and Pyadjoint for measurement of frequency-dependent phase differences estimated with multi-taper approach (Krischer et al., 2015a). For data processing demonstration, we used three-component velocity seismograms from event 3505099 at broadband station KHZ as the observed data. The synthetic data for an initial model were generated from simulations accordingly. Both observed and synthetic velocity data were filtered to a frequency band from f = 0.025 - 0.1 Hz, integrated to displacement then measured to pick sections of good agreement for misfit calculation and adjoint source construction. The short-term average to long-term average ratio (STA/LTA), cross-correlation coefficient (*CC*), travel-time difference (*dT*) and the amplitude anomaly (*dA*) are main criteria for the window selection. Figure 1 (a-c) shows the example of *Pyflex* segmentation for a pair of observed and simulated data. Figure 1 (d-f) shows the adjoint source with corresponding misfit.

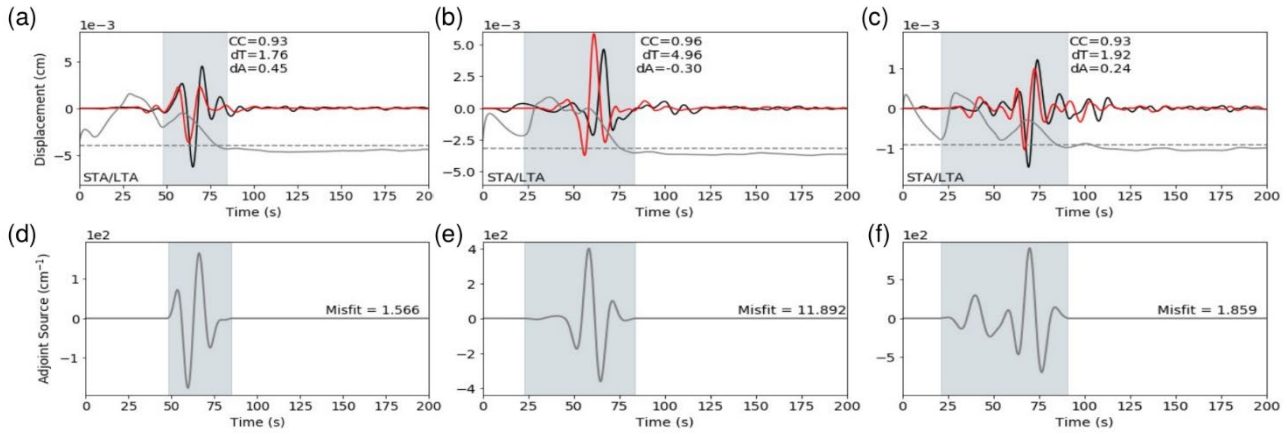

Figure 1: (a-b-c) Three-component displacement seismogram of the observed data (black) and the synthetic data (red) generated from the initial model m00 from broadband station KHZ for event 3505099. Observed seismograms and synthetic seismograms are filtered over the period range 10 to 40s (0.025 to 0.1 Hz). Left column, East-West component (090); center column, North-South component (000); right column, vertical component (ver). Gray-shaded interval presents window picked by Pyflex. (e-d-f): adjoint sources (without time reversal) and misfit calculated by Pyadjoint for the pairs of windowed seismograms above.

3 APPLICATION TO BROADBAND STATION DATA

3.1 Regional context and 3-D velocity models

The region examined in this study is the upper South Island (and Wellington at the bottom of the North Island), as shown in Figure 2. The dimensions of the computational domain are 352 x 352 x 240 km (length x width x depth) which corresponds to 88 x 88 x 60 nodes for a 4 km-spaced grid. The earthquakes located around New Zealand's South Island region are utilized for full waveform inversion of the crustal velocity model. Observed data from 13 earthquakes with Mw = 4.8 - 5.2 and hypocentre varying from 4 to 20 km depth, recorded by 10 broad band stations in the area were included in this study. This set of earthquake events was chosen based on the consistent of the data quality, the source magnitude and the balance of geometrical distribution (Figure 2). A separate independent set of 14 earthquakes (5.2<Mw<6.0) are also used for the purposes of validation to quantify the improvement in waveform misfit metrics from consecutive iterations of inverted velocity models.

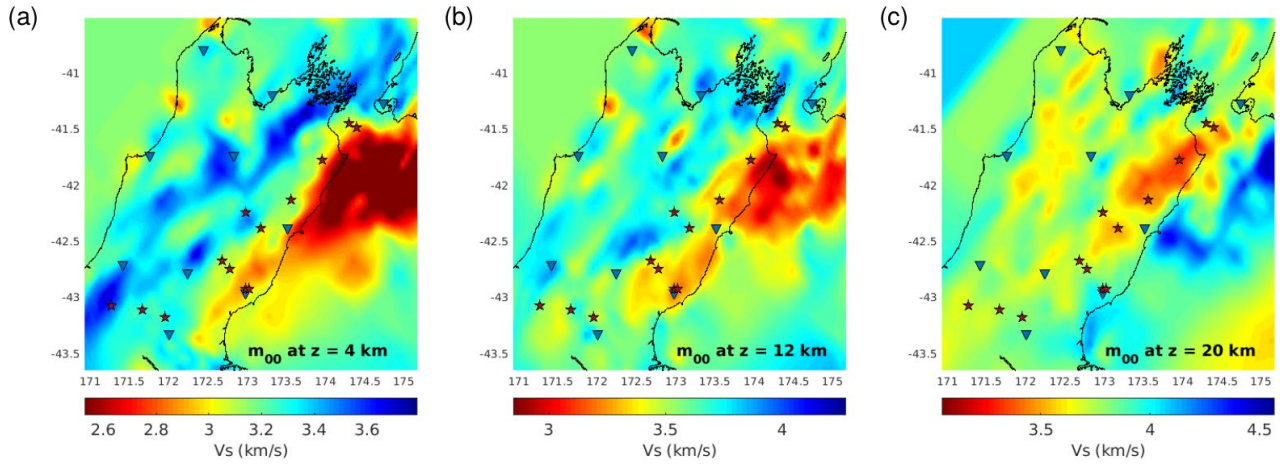

Figure 2: Horizontal planes of shear-wave velocity from the Eberhart-Phillips et al. (2020) velocity model at depths: (a) 4 km; (b) 12 km; and (c) 20 km. Stars are the earthquake events; triangles are the broadband stations.

The observed seismograms were retrieved from GeoNet FDSN channel using *obspy* library (Krischer et al., 2015b). The simulated data were generated using a standard rupture format (srf) source for each event and a given 3-D velocity model. The srf source format defined by an area along the fault plane were generated for forward simulation from a CMT solution provided by GeoNet (Ristau, 2008, 2013) together with a reference 1-D velocity model.

In New Zealand, the 3D crustal velocity models of Eberhart-Phillips et al. (2010, 2020) have been commonly used for wave propagation in recent ground motion studies, including full waveform tomography studies (Chow et al., 2020), and is therefore used as the initial model (m00) in this study. The Eberhart-Phillips et al. (2020) model integrates several regional velocity studies using local earthquakes and onshore recordings of offshore active source data, and has been sequentially updated over the last decade. The model has variable spatial discretization, with fine-scale (<5 km) resolution in areas with high seismicity, such as the Canterbury region, and coarser resolution elsewhere. The model is spatially interpolated onto a regular grid to be used in finite difference calculations utilizing the framework developed by Thomson et al. (2019). Figure 2 also presents three horizontal planes of shear-wave velocity (*Vs*) from the initial velocity model at different depths. The minimum and maximum constraints for *Vs* within the domain are 1.5 km/s and 5.0 km/s, respectively.

3.2 Inversion run using broadband data

Observed data from 13 earthquakes described previously was included in this inversion. Our inversion included 384 three-component seismograms (North-South, East-West and vertical or 090, 000 and ver correspondingly). *Pyflex* has been utilized for segmentation of the observed and synthetic seismograms. The multi-taper approach of misfit calculation and adjoint source construction are performed on windowed sections of the seismograms using *Pyadjoint*. By tuning parameters similar to tomographic scenarios of Southern California (Maggi et al., 2009) as well as New Zealand's scenarios (Chow et al., 2019) and using synthetic data generated from a 3-D velocity model, we are able to pick up segments of the seismograms specified by the start time and end time, cross-correlation coefficient, travel-time difference and the amplitude difference. Only windowed seismograms with normalized correlated coefficient $CC > 0.7$ and maximum time shift $\Delta T < 10$ s are used for inversion to prevent inclusion of erroneous data.

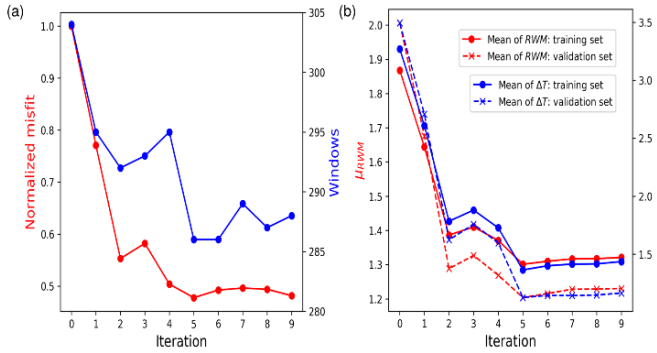

Figure 3: (a) Change of misfit (red) and number of windows (blue) along 9 iterations using 13 events and 384 waveforms; (b) Change of mean for RWM (red) and mean for ΔT (blue) for the training set (solid) and the validation set (dashed).

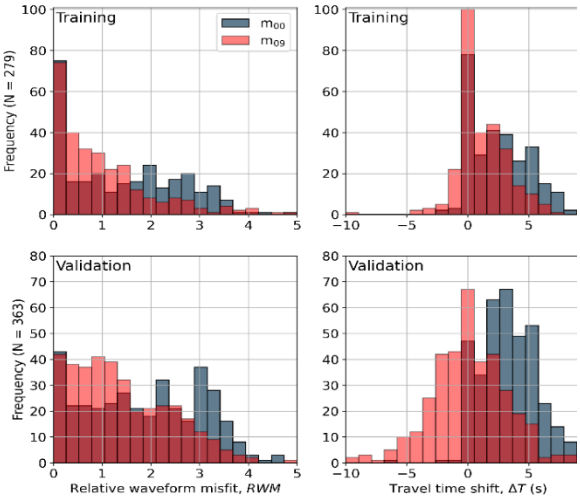

Figure 4: Histograms of RWM (left) and ΔT (right) in corresponding to the initial and inverted model after 10 iterations for 13 events with 279 waveforms included in the tomographic inversion (training set) (top), and for 14 reference events with 363 waveforms not included in the inversion (validation set) (bottom).

After 9 iterations run using L-BFGS method and line search method for determining the update direction and optimal step length, the misfit measuring frequency-dependent phase differences between observed and synthetic data has been reduced by 60% (Figure 3). For validation, we recall the definition of the relative waveform misfit (*RWM*) and travel-time shift (ΔT) based on the normalized cross-correlation coefficient (*NCC*) as Equations (3,4):

$$RWM = \frac{\int_{t_0}^{t_1}[d(t)-s(t)]^2 dt}{\sqrt{\int_{t_0}^{t_1} d(t)^2 dt \int_{t_0}^{t_1} s(t)^2 dt}} \quad (3)$$

$$NCC = \frac{\int_{t_0}^{t_1} d(t-\Delta T)s(t)]^2 dt}{\sqrt{\int_{t_0}^{t_1} d(t)^2 dt \int_{t_0}^{t_1} s(t)^2 dt}} \quad (4)$$

where *d(t)*, *s(t)* are the observed and synthetic data (displacement seismograms); t_0 and t_1 are the start and end time of the window; ΔT is the delay time between observed and synthetic seismogram that maximizes the normalized correlated coefficient.

The histograms of *RWM* and ΔT corresponding to the initial and inverted models after 9 iterations for 13 training events and for 14 validation events are presented in Figure 4. We present our inverted model for *Vs* on both absolute value (Figure 5) and relative change (Figure 6) compared to the initial model for 3 different depths. The variation of shear wave velocities from z = 4 km to 20 km all over the domain ranged from - 41% to +16%.

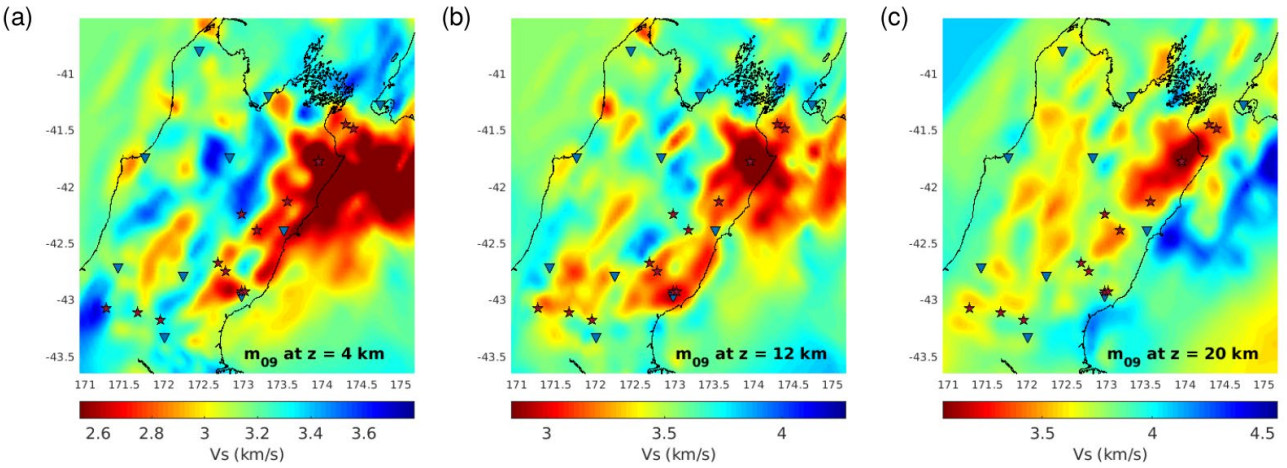

Figure 5: Horizontal cross sections of the inverted Vs model m09 at depths: (a) 4 km; (b) 12 km; and (c) 20 km.

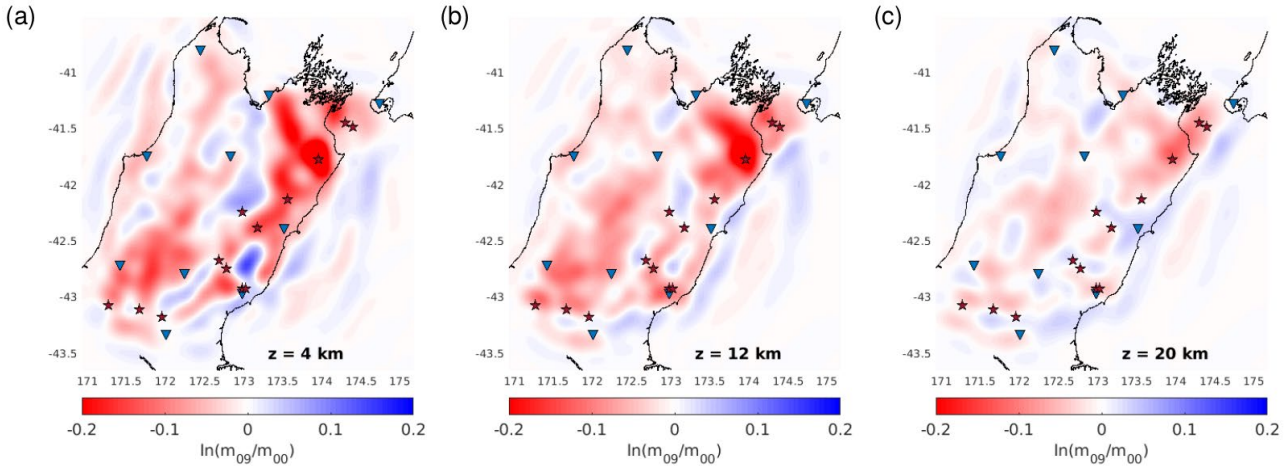

Figure 6: Horizontal cross sections of the change ln(m09/m00) at depths: (a) 4 km; (b) 12 km; and (c) 20 km.

3.3 Waveform improvement and geological interpretation

For waveform comparison and geological interpretation, we project the geological map of the upper South Island (Figure 7a) along with faults, cross-sections and several ray paths (Figure 7b) to the *Vs* and *Vp/Vs* profiles. A waveform comparison (Figure 8) for data recorded at a broadband station (INZ) for a source initiated at the most seismic active area in the North-East (event 2013p544966) are presented with the ray path specified in Figure 8b. The waveform improvement from the initial model to the inverted model after 9 iterations indicates the improvement in the velocity structures as time delays and amplitudes are more similar.

The model m09, which is the final model from the inversion, was chosen for geological interpretation. We used smearing contours where the resolution is 80% of the diagonal element to highlight the area with high contrast in the profiles (Figures 9, 10). Our starting model implies some correlations to the faults/ crustal thickening (Eberhart-Phillips and Bannister, 2010) even though they were not explicitly built into the structural representation. The correlations include the low *Vp/Vs* ratio for the region from Awatere fault to the Porters Pass fault with high crustal seismicity. As a result of tomographic inversion, we observe the magnified *Vp/Vs* ratio contrasts across major faults in our inverted model m09 in the plane view (Figure 9b) and at a cross-section throughout the domain (Figure 10a).

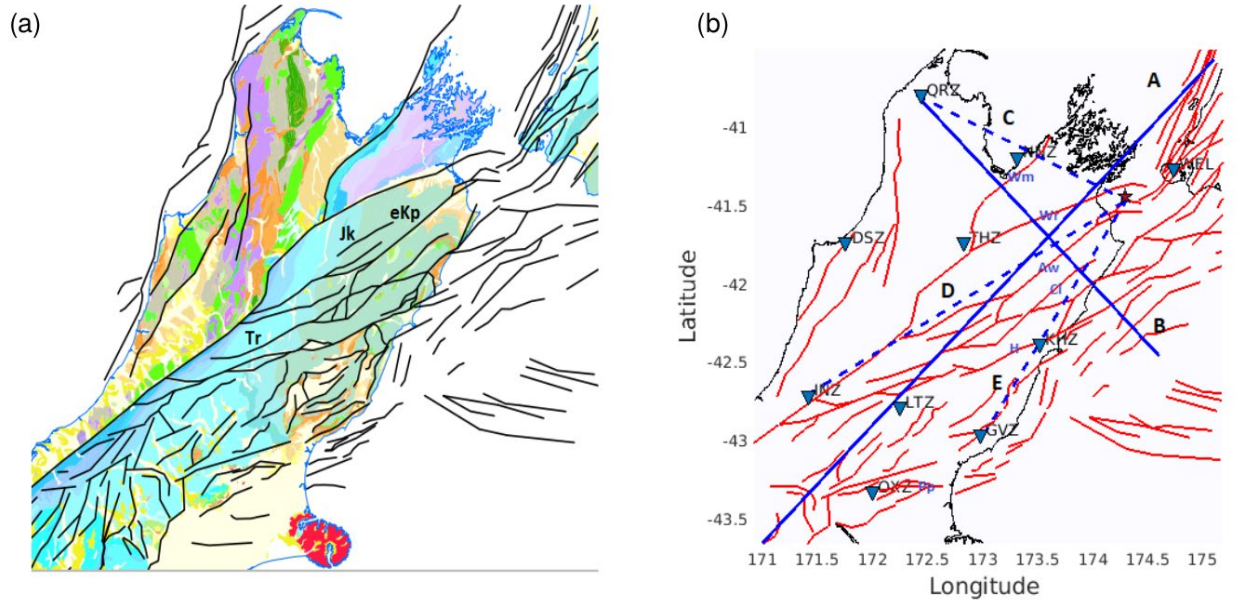

Figure 7: (a) Geological map of the upper South Island, New Zealand (Mortimer, 2004) with some specific features: Pahau Terrane sedimentary rocks (eKp), Rakaia Terrance Triassic sedimentary rock (Tr) and Kaweka Terrance rock (Jk); (b) Maps of broadband stations, cross-sections and raypaths from a specific source (star) and faults including: Wm, Waimea; Wr, Wairau; Aw, Awatere; Cl, Clarence; H, Hope; PP, Porters Pass.

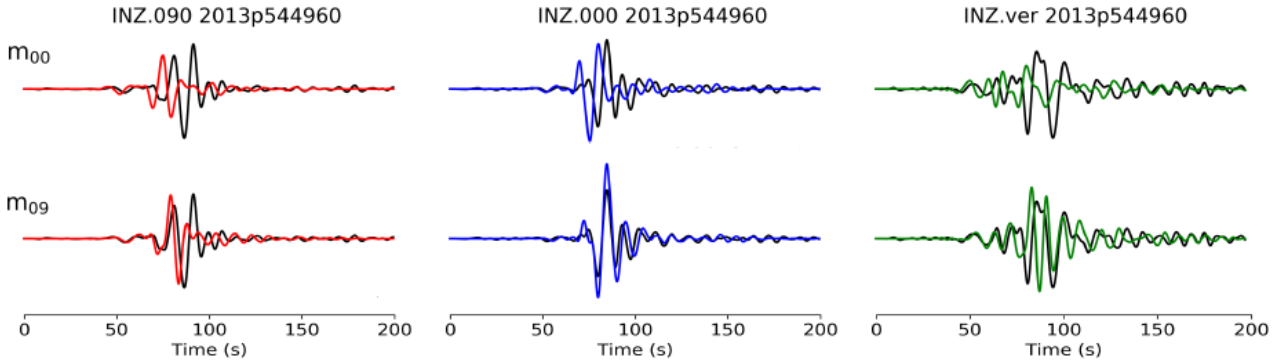

Figure 8: Waveform comparison between the observed data (black) and synthetic data (North-South component (red); East-West component (blue); vertical component (green)) for 2 models m00 and m09 according to event 2013p544960 for station INZ.

From the plane view of *Vp/Vs* ratio at 4 km depth (Figure 9b), the high *Vp/Vs* ratio relates to the occurrence of fluid movement/ seismic activity at the North-East region along the coast and at the South-West area located further North from Arthur's Pass. The faults such as Wairau, Awatere and Hope are observed at the low velocity zones (Figure 10b) and near the boundaries between the low and high *Vp/Vs* ratios (Figure 10a).

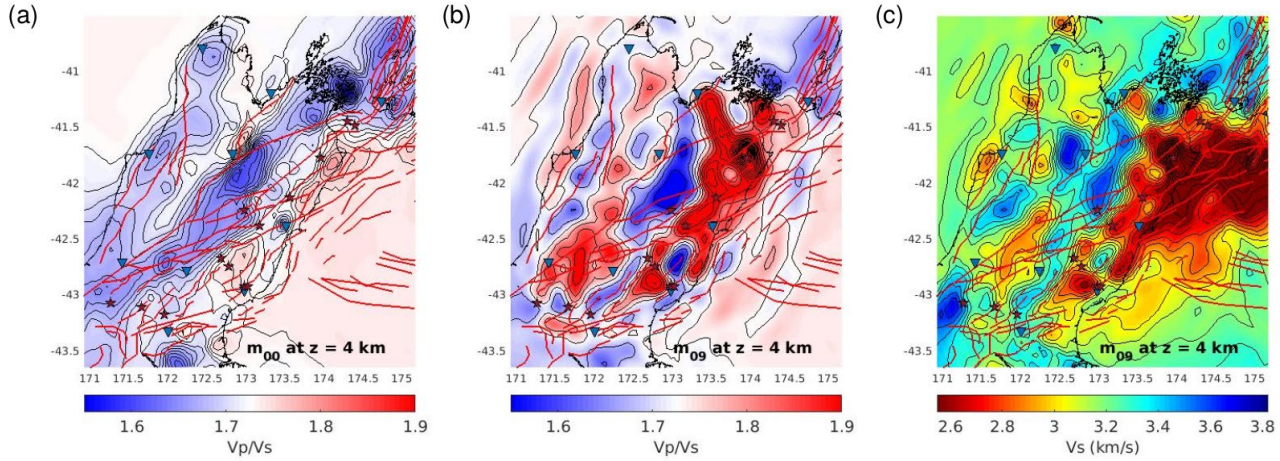

Figure 9: Map views at 4 km - depth of: (a) Vp/Vs according to m00, (b) Vp/Vs according to m09, and (c) Vs according to m09.

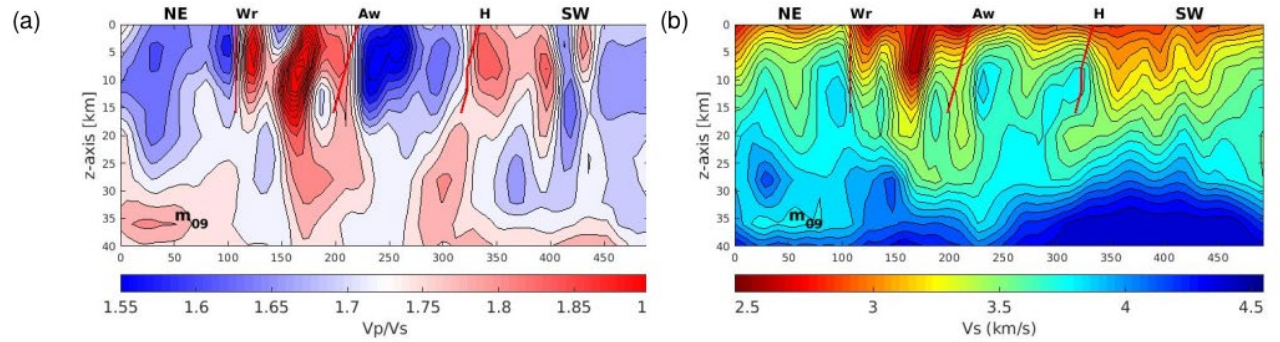

Figure 10: Plane views along the North-East to South-West cross-section: (a) Vp/Vs according to m09 (b) Vs according to m09.

4 CONCLUSIONS

We present an application of full-waveform tomographic inversion of local earthquake data recorded at the broadband stations in the upper South Island, New Zealand. The inversion using full seismic waveform information from the observed data and synthetic data generated according to a 3-D velocity model has iteratively improved the initial model by reducing the defined multi-taper misfit. The inverted model has revealed the high heterogeneity of the crustal structure of the region for the depth from 0 to 20 km which may not be characterized by using traditional travel-time tomography. The resolution of inverted model may be improved in the future by using a larger data set with more seismic stations, finer spatial resolution and higher frequency content of data. Due to the computational efficiency of the current full waveform inversion workflow, the method also can be extended to other parts of New Zealand and jointly incorporated with other existing methods such as ambient noise tomography.

ACKNOWLEDGEMENTS

The numerical simulations were performed on NeSIs high performance computing resources. The work was funded by the University of Canterbury and QuakeCoRE. We thank Donna Eberhart-Phillips for providing New Zealand wide velocity model version 2.2 as the background model included in the tomographic inversion; and GeoNet for the earthquake catalogue and broadband station data used in this study. We also appreciate beneficial discussions with Bryant Chow, Alan Juarez and Carl Tape.

REFERENCES

Bradley, B. A., Bae, S. E., Polak, V., Lee, R. L., Thomson, E. M., and Tarbali, K., 2017. Ground motion simulations of great earthquakes on the Alpine Fault: effect of hypocentre location and comparison with empirical modelling. *New Zealand Journal of Geology and Geophysics* 60, 1–11.

Butzer, S., 2015. 3D elastic time-frequency full-waveform inversion. *Ph.D. thesis*, Verlag nicht ermittelbar.

Chow, B., Kaneko, Y., Modrak, R., Tape, C., and Townend, J., 2019. A semi-automated adjoint tomography workflow applied to New Zealand's North Island. *AGUFM 2019*, S34A–02.

Chow, B., Kaneko, Y., Tape, C., Modrak, R., and Townend, J., 2020. An automated workflow for adjoint tomographywaveform misfits and synthetic inversions for the North Island, New Zealand. *Geophysical Journal International* 223, 1461–1480.

Eberhart-Phillips, D. and Bannister, S., 2010. 3-D imaging of Marlborough, New Zealand, subducted plate and strike-slip fault systems. *Geophysical Journal International* 182, 73–96.

Eberhart-Phillips, D., Bannister, S., and Reyners, M., 2020. Attenuation in the mantle wedge beneath super-volcanoes of the Taupo Volcanic Zone, New Zealand. *Geophysical Journal International* 220,703–723.

Eberhart-Phillips, D., Reyners, M., Bannister, S., Chadwick, M., and Ellis, S., 2010. Establishing a versatile 3-D seismic velocity model for New Zealand. *Seismological Research Letters* 81, 992–1000.

Fichtner, A. and Trampert, J., 2011. Hessian kernels of seismic data functionals based upon adjoint techniques. *Geophysical Journal International* 185, 775–798.

Graves, R., Jordan, T. H., Callaghan, S., Deelman, E., Field, E., Juve, G., Kesselman, C., Maechling, P., Mehta, G., Milner, K. et al., 2011. CyberShake: A physics-based seismic hazard model for southern California. *Pure and Applied Geophysics* 168, 367–381.

Graves, R. and Pitarka, A., 2015. Refinements to the Graves and Pitarka (2010) broadband groundmotion simulation method. *Seismological Research Letters* 86, 75–80.

Graves, R. W., 1996. Simulating seismic wave propagation in 3D elastic media using staggered-grid finite differences. *Bulletin of the Seismological Society of America* 86, 1091–1106.

Krischer, L., Fichtner, A., Zukauskaite, S., and Igel, H., 2015a. Large-scale seismic inversion framework. *Seismological Research Letters* 86, 1198–1207.

Krischer, L., Megies, T., Barsch, R., Beyreuther, M., Lecocq, T., Caudron, C., and Wassermann, J.,2015b. ObsPy: A bridge for seismology into the scientific Python ecosystem. *Computational Science & Discovery* 8, 014003.

Laske, G. and Masters, G., 1996. Constraints on global phase velocity maps from long-period polarization data. Journal of Geophysical Research: *Solid Earth* 101, 16059–16075.

Lee, E.-J., Chen, P., Jordan, T. H., Maechling, P. B., Denolle, M. A., and Beroza, G. C., 2014. Full 3-D tomography for crustal structure in southern California based on the scattering-integral and the adjoint-wavefield methods. Journal of Geophysical Research*: Solid Earth* 119, 6421–6451.

Maggi, A., Tape, C., Chen, M., Chao, D., and Tromp, J., 2009. An automated time-window selection algorithm for seismic tomography. *Geophysical Journal International* 178, 257–281.

Modrak, R. T., Borisov, D., Lefebvre, M., and Tromp, J., 2018. SeisFlowsFlexible waveform inversion software. *Computers & geosciences* 115, 88–95.

Mortimer, N., 2004. New Zealand's geological foundations. *Gondwana research* 7, 261–272.

Nocedal, J. and Wright, S., 2006. Numerical optimization. *Springer Science & Business Media*.

Plessix, R.-E., 2006. A review of the adjoint-state method for computing the gradient of a functional with geophysical applications. *Geophysical Journal International* 167, 495–503.

Ristau, J., 2008. Implementation of routine regional moment tensor analysis in New Zealand. *Seismological Research Letters* 79, 400–415.

Ristau, J., 2013. Update of regional moment tensor analysis for earthquakes in New Zealand and adjacent offshore regions. *Bulletin of the Seismological Society of America* 103, 2520–2533.

Shin, C., Jang, S., and Min, D.-J., 2008. Improved amplitude preservation for prestack depth migration by inverse scattering theory. *Geophysical prospecting* 49, 592–606.

Tape, C., Liu, Q., Maggi, A., and Tromp, J., 2009. Adjoint tomography of the southern California crust. *Science* 325, 988–992.

Tape, C., Liu, Q., Maggi, A., and Tromp, J., 2010. Seismic tomography of the southern California crust based on spectral-element and adjoint methods. *Geophysical Journal International* 180, 433–462.

Tape, C., Liu, Q., and Tromp, J., 2007. Finite-frequency tomography using adjoint methods Methodology and examples using membrane surface waves. *Geophysical Journal International* 168, 1105–1129.

Tarantola, A., 1984. Inversion of seismic reflection data in the acoustic approximation. Geophysics 49, 1259–1266.

Thomson, E. M., Bradley, B. A., and Lee, R. L., 2019. Methodology and computational implementation of a New Zealand Velocity Model (NZVM2. 0) for broadband ground motion simulation. *New Zealand Journal of Geology and Geophysics* pp. 1–18.

Tran, K. T., Nguyen, T. D., Hiltunen, D. R., Stokoe, K., and Menq, F., 2020. 3D full-waveform inversion in time-frequency domain: Field data application. *Journal of Applied Geophysics* p. 104078.

Tromp, J., Tape, C., and Liu, Q., 2005. Seismic tomography, adjoint methods, time reversal and bananadoughnut kernels. *Geophysical Journal International* 160, 195–216.

Virieux, J., 1986. P-SV wave propagation in heterogeneous media; velocity-stress finite-difference method. *Geophysics* 51, 889–901.

Zhu, H., Bozda˘g, E., and Tromp, J., 2015. Seismic structure of the European upper mantle based on adjoint tomography. *Geophysical Journal International* 201, 18–52.